

Modified Lamb Wave Delay Factor-Based Multiply-Sum Probabilistic Diagnostic Imaging Algorithm of Composite Structures

Lingyu Sun^{ID}, Juntao Wei^{ID}, Chang Peng^{ID}, Zengye Ju^{ID}, Shanshan Lv^{ID}, Faye Zhang^{ID}, Lei Zhang^{ID}, Lei Jia^{ID}, and Mingshun Jiang^{ID}, Member, IEEE

Abstract—Ultrasonic guided wave (UGW) imaging technology has been extensively adopted to assess the structural performance of composite laminates for its high detection accuracy, quick speed, and real-time detection capability. However, the algorithm design in composite structures is hindered by the complexity and anisotropy of dispersion. It is still challenging to optimize localization and detection range in sparse sensing arrays though the probabilistic diagnostic imaging (PDI) method avoids precise signal analysis. In this study, a modified delay-factor-based multiply-sum PDI (MDF-MSPDI) algorithm is examined. A novel ring-shaped probability distribution function based on the delay characteristics of damage scattering is defined, such that the off-axis localization and tolerance capabilities of the classical PDI method are enhanced. Subsequently, the delayed item is modified using the directional correlation of the group velocity in composite structures. Furthermore, given the spatial coherence of the path probability data, the new probability distribution terms are built through the nonlinear multiply-sum operation of path imaging to eliminate pointless damage artifacts and effects exerted by computational error. Finally, the algorithm performance was verified through simulated damage and impact damage experiments on composite laminates. As indicated by the result, the proposed algorithm exhibits excellent localization capability for damage in the internal and edge of the sensing arrays.

Index Terms—Laminated composites, modified delay factor (MDF), multiply-sum probabilistic diagnostic imaging (MSPDI), structural health monitoring (SHM), ultrasonic guided wave (UGW).

I. INTRODUCTION

CARBON fiber composites have been extensively used in several fields (e.g., aerospace, rail transportation, and

Manuscript received 25 December 2022; revised 21 March 2023; accepted 28 March 2023. Date of publication 19 April 2023; date of current version 15 May 2023. This work was supported in part by the National Key Research and Development Project through the General Program under Grant 2020YFE0204900; in part by the National Natural Science Foundation of China through the General Program under Grant 62073193, Grant 61903224, Grant 62273206, and Grant 61873333; and in part by the Key Research and Development Plan of Shandong Province through the General Program under Grant 2019TSLH0301 and Grant 2021CXGC010204. The Associate Editor coordinating the review process was Dr. Bruno Albuquerque De Castro. (*Corresponding author: Mingshun Jiang*)

Lingyu Sun, Juntao Wei, Shanshan Lv, Faye Zhang, Lei Zhang, Lei Jia, and Mingshun Jiang are with the School of Control Science and Engineering, Shandong University, Jinan 250061, China (e-mail: sunlingyu@sdu.edu.cn; weijuntao1992@126.com; lvshanshan@sdu.edu.cn; zhangfaye@sdu.edu.cn; drleizhang@sdu.edu.cn; jialei@sdu.edu.cn; jiangmingshun@sdu.edu.cn).

Chang Peng and Zengye Ju are with the Zhongche Qingdao Sifang Locomotive and Rolling Stock Company Ltd., Qingdao 266111, China (e-mail: pengchangcqu@gmail.com; youyolumingsyzp@163.com).

Digital Object Identifier 10.1109/TIM.2023.3268447

new energy), for their excellent properties (e.g., lightweight, high specific strength, excellent structural integrity, and design ability) [1]. It has achieved wide applications in the fuselage and wings of aircraft, the body structure of satellites and communication antennas, and so forth. Moreover, structures (e.g., train bodies and bogie frames) have started to use composites for weight reduction and performance improvement. Fiber-reinforced composites are subjected to complex damage (e.g., matrix cracking, delamination, debonding, and fiber fracture internally under cyclic fatigue loading), differing from metallic materials [2], [3]. In general, the above-described damage forms occur in a single or combined manner. Besides, they are significantly correlated with the structural material, lay-up properties, and external loading effects. As a result, the residual material strength and structural load carrying capacity will be reduced, posing a significant safety hazard [4]. Accordingly, the monitoring and assessing the structural properties of composite laminates have been a contentious topic of great interest.

The ultrasonic guided wave (UGW)-based structural health monitoring (SHM) technique has been confirmed to be promising in nondestructive testing (NDT) of composite laminates for its advantages of wide detection range, good damage sensitivity, and the possibility of online monitoring [5], [6]. This technique conforms to a principle as follows: the generation of damage in a solid plate-like medium will lead to the changes in the boundary conditions or the position of the center of mass, such that the reflection and scattering phenomena of the UGW are generated. The damage scattering effect acts on the direct wave and may be manifested in the response signal as several behaviors (e.g., directional deflection, phase shift, amplitude attenuation, and harmonic generation) [7]. UGW is excited and captured by piezoelectric transducer (PZT) arrays in ultrasound imaging technology. It serves as a carrier and transmission medium of damage information to visualize structural damage by comparing the baseline signal and response signal characteristics. In general, the probabilistic tomography (PT) [8], the phased-array (PA) [9], the delay and sum (DAS) [10], the sparse reconstruction (SR) [11], the probability diagnostic imaging (PDI) [12], and other methods have been proposed to address the problem of damage imaging. To be specific, the path-imaging-based PDI method and the damage delay-principle-based DAS method have aroused the most extensive attention.

The PDI method refers to a fast damage reconstruction algorithm that exhibits high tolerance and stability. However, the imaging capability of PDI is limited by numerous factors (e.g., damage index, probability distribution function, density of sensing arrays, and ellipsoidal scaling factor). The damage index represents the intensity of the signal change arising from the damage. With the deepening of the relevant research, characterization methods for damage index (e.g., correlation factor (CF) [13], time of flight (TOF) [14], energy factor (EF) [15], and information entropy (IE) [16]) have been progressively developed. The probability distribution function is adopted to characterize the degree of effect of the damage on the path. It is generally defined in accordance with a linearly decreasing degree of the relative distance between the pixel point and the path. The function requires the definition of a scaling parameter β , and it is adopted to regulate the range and decay rate of the damage distribution. Notably, experience and several tests take on critical significance to this function when it carries out a fuzzy selection in a suitable interval without a definite selection criterion [17]. Several methods have been adopted in recent research to account for β . Wu et al. [18] proposed an optimal scaling parameter selection method based on optimized networks and unit weight regions. Jin et al. [8] proposed a modified PT (MPT) method with variable shape factor β at the respective damage path to quantitatively represent the expansion of the defect region. It is noteworthy that the PDI algorithm will reinforce the damage probability of path or path intersections, which is not friendly for the area of non-paths. Accordingly, denser sensing arrays are required to cover more damaged areas to improve the imaging quality, thus causing increased costs. In this case, Huo et al. [19] proposed an elliptical probabilistic imaging method based on a Bayesian framework to increase the imaging resolution in composite plates. Liu et al. [20] corrected the weight distribution function by obtaining the relative distance from the defect to all actuator-receiver pairs and narrowing the weight distribution area. Zhang et al. [21] proposed a semi-supervised deep convolutional neural network probabilistic imaging algorithm (DCNN-PIA) to extract the damage index automatically. Furthermore, Wang et al. [22] suggested that the confidence level of the algorithm will be elevated when data fusion involves more damaged sensing paths, and they developed a virtual sensing path method.

In contrast, the DAS method achieves accurate imaging by building and accumulating backpropagating elliptical damage trajectories. This method is effective in overcoming the lack of off-axis localization capability of the PDI method, thus that it is endowed with an ability to detect large-area structures using sparse sensing arrays quickly. Initially, the idea of focusing the delayed signal backward was proposed by Wang et al. [23] and developed by Michaels et al. [24]. Gradually, it was applied to identifying and localizing damage (e.g., impacts [25] and cracks [26]). However, for anisotropic material, the directional difference of the UGW dispersion velocity cannot be ignored. Existing research has been conducted on slowness map model-based numerical simulations [25], [27]. Nevertheless, the prior knowledge the method relies on

(e.g., dispersion, group velocity, and TOF) will be biased due to the unknown nature of the material modulus parameters and the interference of theoretical approximation errors, and it will trigger large speckles or artifacts in the reconstructed image. Thus, it is essential to implement an algorithmic tolerance or denoising design to obtain precision. Methods (e.g., multi-signal classification (MUSIC) [28], minimum variance imaging (MVDR) [29], Gaussian mixture model (GMM) [30], and coordinate transformation [31]) have been adopted to suppress the interference of noise or time-varying factors to improve the imaging quality.

In this study, a modified delay-factor-based multiply-sum probabilistic diagnostic imaging (MDF-MSPDI) algorithm is proposed, such that the composite structure positioning accuracy and the detection range are improved. First, the idea of signal delay in DAS is added to formulating a probability distribution of PDI to enhance the off-axis positioning ability. Subsequently, the anisotropic group velocity model of the composite structure is built based on the numerical simulation and experimental verification. Next, given the path space coherence of damage imaging, the idea of multiplying cumulative beamforming applied to the medical ultrasound field is introduced [32], [33]. A nonlinear superposition between paths is performed to form the damage probability distribution. Finally, the higher order mode of the algorithm is given to ensure the imaging quality.

The remaining sections of this article are organized as follows. Section II introduces the theoretical background and methodology, including the constitutive properties of composite structures, the propagation properties of UGW, and the principle of the proposed algorithm. Section III describes the experimental setup and illustrates the steps of simulated and impact damage experiments. Section IV shows the process of signal processing and parametric analysis based on pre-experiment data. Section V assesses and discusses the algorithm's performance based on extensive experimental data. Finally, conclusions are drawn in Section VI.

II. THEORY BACKGROUND AND METHODOLOGY

A. Constitutive Equation of Composite Plate

For linearly elastic materials, the stress-strain relationship is usually expressed in terms of generalized Hooke's law as follows:

$$\sigma_{ij} = c_{ijkl}\varepsilon_{kl} \quad (1)$$

where σ_{ij} is the stress tensor, ε_{kl} is the strain tensor, and c_{ijkl} is the fourth-order stiffness tensor for anisotropic materials.

As depicted in Fig. 1, the global coordinate system X-Y-Z is defined in accordance with the observed direction of UGW propagation. The local coordinate system x-y-z is defined based on the fiber's laying angle ϕ in the global coordinate system. In general, composite laminates used in engineering serve as transversely isotropic materials. Only five independent constants exist in stiffness matrix C_{mn} due to the symmetry of the material, which are usually defined in the local coordinate

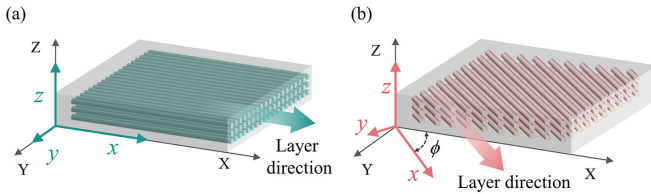


Fig. 1. Global and local coordinate systems for composite laminates: (a) $\phi = 0$ and (b) $\phi \neq 0$.

system as follows:

$$\mathbf{C}_{mn} = \begin{bmatrix} C_{11} & C_{12} & C_{13} & 0 & 0 & 0 \\ C_{12} & C_{22} & C_{23} & 0 & 0 & 0 \\ C_{13} & C_{23} & C_{33} & 0 & 0 & 0 \\ 0 & 0 & 0 & C_{44} & 0 & 0 \\ 0 & 0 & 0 & 0 & C_{55} & 0 \\ 0 & 0 & 0 & 0 & 0 & C_{66} \end{bmatrix}. \quad (2)$$

The tensor components of the matrix can be determined from the experimentally measured elastic constants E_i (Young's modulus in the i -direction), v_{ij} (Poisson's ratio), and G_{ij} (shear modulus in the j -direction) [34].

When $\phi = 0$ [Fig. 1(a)], the global coordinate system is consistent with the local coordinate system. When $\phi \neq 0$ [Fig. 1(b)], the stiffness matrix \mathbf{C} in the global coordinate system is expressed as follows:

$$\mathbf{C} = \mathbf{T}_C^{-1} \mathbf{C}_{mn} \mathbf{T}_C^T \quad (3)$$

where the superscript -1 denotes the matrix inverse, the superscript T represents the transpose of the matrix, and \mathbf{T}_C expresses the transpose matrix of lay-up angle ϕ

$$\mathbf{T}_C = \begin{bmatrix} u^2 & w^2 & 0 & 0 & 0 & 2uw \\ w^2 & u^2 & 0 & 0 & 0 & -2uw \\ 0 & 0 & 1 & 0 & 0 & 0 \\ 0 & 0 & 0 & u & -w & 0 \\ 0 & 0 & 0 & w & u & 0 \\ -uw & uw & 0 & 0 & 0 & u^2 - w^2 \end{bmatrix} \quad (4)$$

where $u = \cos(\phi)$, $w = \sin(\phi)$. It can be seen that the UGW dispersion of the composite laminate is affected by lay-up angle ϕ . The difference in UGW's direction will cause differences in the group velocity and the phase velocity.

B. Lamb Wave in Composite Laminates

UGW refers to an elastic wave generated by the motion of a plasmon in a solid plate or layer, and the equation of motion of the plasmon can effectively express this behavior [35]. Lamb waves propagate within a structure in both the symmetric (S) and antisymmetric (A) modes, accompanied by the generation of multimode phenomena (S0, S1, S2, etc. and A0, A1, A2, etc.).

The propagation pattern of Lamb waves in multilayer structures is highly complex. Solving the fluctuation equations to capture the Lamb waves' characteristics in composite laminates is still challenging. Accordingly, with the help of the open-source dispersion calculator (DC), we simulated the dispersion curve for a composite laminate with a lay-up of

TABLE I

MATERIAL ELASTICITY PARAMETERS

Density (kg/m ³)	E1 (GPa)	E2 (GPa)	E3 (GPa)	G12 (GPa)	G13 (GPa)	G23 (GPa)	ν_{12}	ν_{13}	ν_{23}
1750	131	9	9	4.5	4.5	3.36	0.3	0.3	0.34

TABLE II

TENSOR COMPONENTS OF THE STIFFNESS MATRIX

C11 (GPa)	C12 (GPa)	C13 (GPa)	C22 (GPa)	C23 (GPa)	C33 (GPa)	C44 (GPa)	C55 (GPa)	C66 (GPa)	ν_{23}
133.5	4.2	4.6	10.3	3.6	10.3	4.5	5.4	5.4	0.34

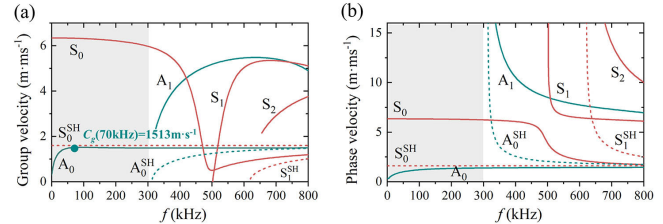


Fig. 2. Dispersion curve of the composite laminate along the 0° direction: (a) group velocity curve and (b) phase velocity curve.

$[0^\circ/90^\circ]_6$ and a thickness of 2.4 mm. The elastic constants of the material are shown in Table I. Tensor components of the stiffness matrix are calculated (Table II).

The proposed method needs to calculate the TOF of guided waves, so the obtained signal should meet the following conditions: significant capture of A0 mode, which requires reasonable frequency selection under the guidance of the dispersion curve. Fig. 2 presents the group velocity and phase velocity dispersion curves for symmetric, antisymmetric Lamb waves, and horizontal shear waves in the 0° direction. In the low-frequency range below 300 kHz, only S0 and A0 modes will be generated and propagate with almost constant velocity. It is often referred to as the nondispersive region where dispersion is negligible. In this interval, the separation of the modes is improved with the increase in the velocity difference. Moreover, with the decrease in the frequency, the energy attenuation effect of the UGW will decline, thus facilitating signal analysis. As a result, the selection of excitation frequency is restricted to the low-frequency range, and 70 kHz serves as an example for algorithm design and verification.

Furthermore, as depicted in Fig. 3, the group velocity curve of A0 mode at 70 kHz is determined and then fit to obtain the group velocity modification function (5). As indicated by the result, the UGW achieves the maximum velocity in the 0° direction. The group velocity will generate significant differences with the change in the propagation angle. Accordingly, the modification of velocity takes on a critical significance to composite structures

$$f(\theta) = 1404 + 86 \left(\sin \left(\frac{\pi(\theta + 96)}{184} \right) \right)^2, \quad 0 \leq \theta \leq 360. \quad (5)$$

C. Modified Delay Factor

The scattering signal carries important damage information. For the i th path, the scattered signal is obtained by subtracting

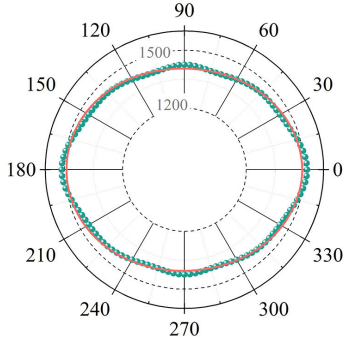


Fig. 3. Group velocity in all the directions at 70 kHz after fitting.

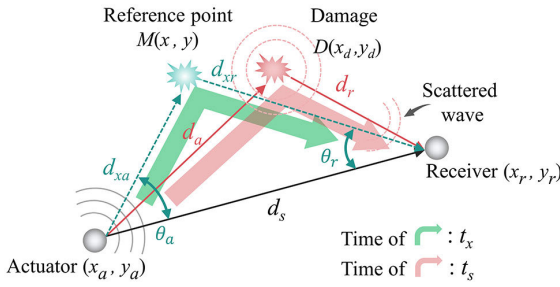


Fig. 4. Time delay principle of damage scattering signal.

the damage signal from the baseline signal

$$s_i = c_i - b_i \quad (6)$$

where c_i is the response signal in damaged structures, b_i is the baseline signal in healthy structures, and s_i is the scattered signal. The damage's actual arrival time t_{si} is the TOF of s_i .

For isotropic materials, Fig. 4 illustrates the principle of backpropagation of the UGW from actuator $A(x_{ai}, y_{ai})$ to receiver $R(x_{ri}, y_{ri})$ through a reference point $M(x, y)$ in the plane. The reference damage's arrival time t_{xi} is written as follows:

$$\begin{aligned} t_{xi} &= \frac{d_{xai} + d_{xri}}{c_g} \\ &= \frac{\sqrt{(x - x_{ai})^2 + (y - y_{ai})^2} + \sqrt{(x - x_{ri})^2 + (y - y_{ri})^2}}{c_g} \end{aligned} \quad (7)$$

where d_{xai} denotes the distance from A to M; d_{xri} represents the distance from M to R; c_g expresses the group velocity, which can be easily measured from dispersion curve or experiments.

For anisotropic materials, substituting the average velocity \bar{c}_g into (7) to calculate the delay factor (DF) may introduce errors for ignoring the directional variations. The accumulation of velocity differences will increase the errors with the sensing path's length grows, failing to meet the requirements of a broader range of monitoring. Thus, the group velocity should be modified to obtain more accurate positioning, and (7) is

written as follows:

$$\begin{aligned} t_{xi} &= t_{xai} + t_{xri} \\ &= \frac{\sqrt{(x - x_{ai})^2 + (y - y_{ai})^2}}{c_{ga}} + \frac{\sqrt{(x - x_{ri})^2 + (y - y_{ri})^2}}{c_{gr}} \end{aligned} \quad (8)$$

where t_{xai} and t_{xri} are the times UGW propagates from A to M and from M to R. c_{ga} and c_{gr} are the velocity that UGW propagates from A to M and from M to R, respectively, which can be obtained from the following equation:

$$c_{ga} = f(\theta_a), \quad \theta_a = \arctan\left(\frac{y - y_{ai}}{x - x_{ai}}\right) \quad (9)$$

$$c_{gr} = f(\theta_r), \quad \theta_r = \arctan\left(\frac{y_{ri} - y}{x_{ri} - x}\right). \quad (10)$$

The modified DF (MDF) τ_d is defined to measure the probability of damage

$$\tau_d = \left| \frac{t_x - t_s}{t_s} \right| \quad (11)$$

where t_s is the TOF of the scattered signal's A0 mode. The smaller the τ_d , the closer the actual damage point will be to reference point M, and the greater the possibility of damage at M will be. The larger the τ_d , the less the possibility of damage at M will be.

D. MDF-PDI

For any path, if the distance of the signal scattered from the actuator through the damage to the receiver is a fixed value d_s , the damage can be approximately determined on an ellipse. The PDI method sums the elliptical probability distributions based on the sensor pairs to form an overall probability distribution related to the damage. For n sensors in the plane, the number of sensing paths is as presented follows:

$$N = \frac{n(n+1)}{2}. \quad (12)$$

The overall damage probability distribution is defined as follows:

$$y_{PDI}(x, y) = \sum_{i=1}^N p_i(x, y). \quad (13)$$

The image is divided into numerous pixel grids at a scale of 1×1 mm. For i th path, the damage probability distribution at any one reference point in the grid is

$$p_i(x, y) = C_{fi} \cdot W_i(x, y) \quad (14)$$

where $W(x, y)$ denotes the probability distribution function; C_f represents the weighting factor, which is adopted to reinforce the degree of damage to a particular path. It can be defined as follows:

$$C_{fi} = 1 - \rho(b_i, c_i) \quad (15)$$

where $\rho(b_i, c_i)$ denotes the correlation coefficient between the i th baseline signal b_i and the i th damage signal c_i , which can be defined as follows:

$$\rho(b_i, c_i) = \frac{\sum_{k=1}^K (b_{ik} - \bar{b}_i)(c_{ik} - \bar{c}_i)}{\sqrt{\sum_{k=1}^K (b_{ik} - \bar{b}_i)^2 \sum_{k=1}^K (c_{ik} - \bar{c}_i)^2}} \quad (16)$$

公式是否有问题

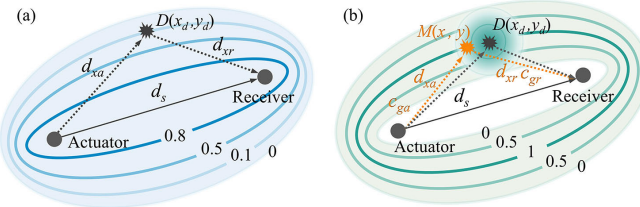


Fig. 5. Schematic of the probability distribution: (a) PDI and (b) MDF-PDI.

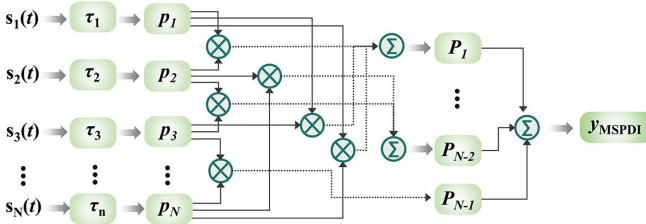


Fig. 6. Flowchart of the calculation of the MSPDI algorithm.

where k denotes the sequence number of discrete points; K represents the number of sampling points; \bar{b}_i and \bar{c}_i express the average amplitude of b_i and c_i , respectively.

The classic PDI method defines the damage probability distribution by capturing the elliptic **intercept** of the distance factor [Fig. 5(a)]. However, some problems should be addressed. On one hand, the damage probability at the path and the path's intersection is enhanced. On the other hand, the imaging result is strongly affected by the decay rate of the scaling parameter β and should be selected carefully. **Accordingly, we propose a novel damage probability distribution method based on MDF, as shown in Fig. 5(b).** The coordinates corresponding to the minimum value of τ_d are defined as the most likely position for damage to occur. Thus, the localization accuracy depends on τ_d instead of β .

The probability distribution function is defined as follows:

$$W_i(x, y) = \begin{cases} 1 - \frac{1}{\beta} \cdot \tau_d, & \tau_d < \beta \\ 0, & \tau_d \geq \beta. \end{cases} \quad (17)$$

E. Modified Delay-Factor-Based Multiply-Sum Probabilistic Diagnostic Imaging

Affected by noise, the classical PDI algorithm still has shortcomings in imaging accuracy and stability. Referring the ideas of delay multiplication and beam formation of radar systems and medical ultrasound, we propose a new nonlinear multiply-sum probabilistic imaging method named multiply-sum probabilistic diagnostic imaging (MSPDI). The signals are coupled and multiplied prior to linear superposition, and Fig. 6 illustrates the relevant principle.

For any damage $M(x, y)$ in the plane, the MSPDI algorithm can be expressed as follows:

$$y_{\text{MSPDI}} = \sum_{i=1}^{N-1} \sum_{j=i+1}^n p_{ij}(\tau_d) \quad (18)$$

这里n是什么
sign是什么运算符?

$$p_{ij}(\tau_d) = \text{sign}(p_i(\tau_d)p_j(\tau_d)) \cdot \sqrt{|p_i(\tau_d)p_j(\tau_d)|} \quad (19)$$

where $p_i(\tau_d)$ and $p_j(\tau_d)$ are the weighted probability distribution functions for the i th and j th receivers. Equation (18) can be expanded to express as follows:

$$\begin{aligned} y_{\text{MSPDI}} = & \underbrace{p_1 \cdot (p_2 + p_3 + p_4 + \cdots + p_{N-1} + p_N)}_{P_1} \\ & + \underbrace{p_2 \cdot (p_3 + p_4 + \cdots + p_{N-1} + p_N)}_{P_2} \\ & + \cdots + \underbrace{p_{N-2} \cdot (p_{N-1} + p_N)}_{P_{N-2}} \\ & + \underbrace{p_{N-1} \cdot p_N}_{P_{N-1}}. \end{aligned} \quad (20)$$

Each term in (20) is viewed as a new probability distribution

$$P_i = p_i \cdot \sum_{j=i+1}^N p_j, \quad \text{for } 1 \leq i \leq N-1. \quad (21)$$

For some structures, performing a single MSPDI operation is not enough to obtain clear and accurate imaging results. In this case, a double-stage (DS) operation can be performed after the new signal y_{MSPDI} to produce a higher order output $y_{\text{DS-MSPDI}}$

$$y_{\text{DS-MSPDI}} = \sum_{i=1}^{N-1} \sum_{j=i+1}^N P_i \cdot P_j. \quad (22)$$

The algorithm performs a nonlinear multiplication operation, which can be interpreted as an **aperture** autocorrelation function. It represents the spatial correlation between all the receiver signals at the respective moment. Compared with classic PDI methods, it is more robust to outliers and noise. However, higher order calculation will bring more workload while improving the accuracy. Thus, a tradeoff between time loss and imaging accuracy should be considered during the selection of the optimal order of the algorithm.

F. Framework of the Research

The framework diagram of the proposed algorithm in this study is shown in Fig. 7, and the main steps are as follows:

Step 1 (Signal Acquisition): The experimental system is built, the sensing arrays are designed, the sensor coordinates are collected, and the UGW response signals in the nondestructive and damaged structures are acquired as the inputs.

Step 2 (DF Modification): The effective path is optimized by scattering energy accumulation parameter E_0 (24) and threshold α . The group velocity modification function is obtained experimentally, and the result is verified through numerical simulation. The MDF is calculated, and then it enters the next step.

Step 3 (MSPDI Algorithm Implementation): The selection principles of the scaling parameters β are determined based on the path's probabilistic imaging p_N . The multiply-sum operation of coupled p_N is performed, the double-stage output is calculated, and the optimal order is verified.

Step 4 (Output and Assessment): The peak point of imaging is recognized as the damage position. Mean absolute error (MAE) and standard deviation (STD) are defined to assess algorithm performance.

前文
未提及

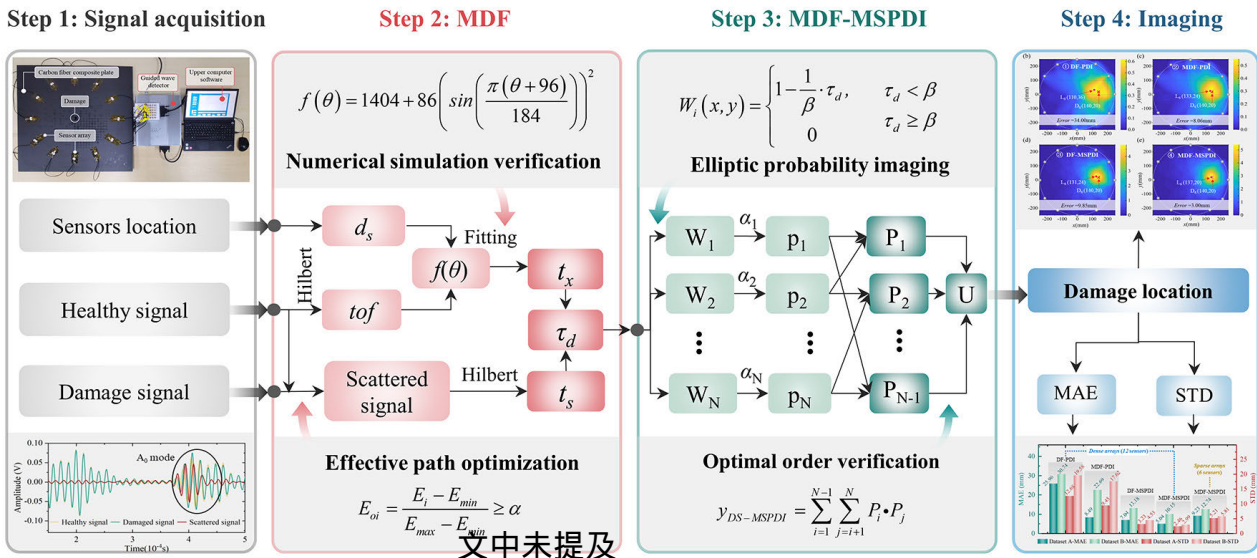


Fig. 7. Framework of the proposed method.

Gain是什么

TABLE III
INFORMATION OF EXPERIMENTAL SYSTEM AND SENSORS

Information of experimental system		Information of sensors	
Frequency range	60kHz-1MHz	Material	Lead zirconate titanate
Voltage range	±80 V	Size(diameter/thickness)	8mm/0.5mm
Sampling frequency	10MSPS	ε	1600
Gain	30dB	d33	≥ 600

Million Samples per Second

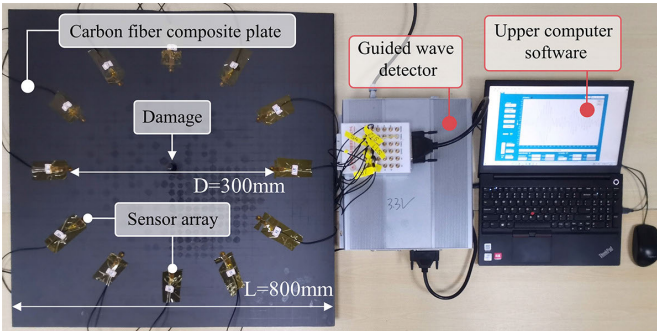


Fig. 8. UGW experimental setup.

III. EXPERIMENT

A. UGW Experimental Setup

The damage detection system was built to verify the effectiveness of the proposed method. The system consists of a composite plate and a self-developed ultrasound guided wave detector (Fig. 8). The upper computer software is capable of controlling the UGW detector, polling excitation, and reception of multichannel Lamb waves. A total of 12 PZT sensors, termed S1–S12, were glued to a composite plate with epoxy resin to develop a ring sensing array. A square composite laminate served as the specimen with a lay-up of [0°/90°]_{6s} (Fig. 9). Table III lists the information regarding the experimental systems and sensors.

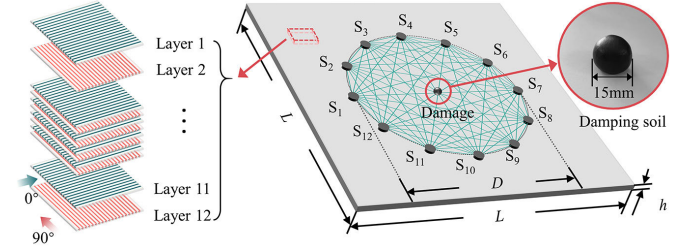


Fig. 9. Details of the plate to be measured.

TABLE IV
COORDINATES OF PZT SENSORS PASTED ON (UNIT: mm)

Sensor	Coordinate	Sensor	Coordinate	Sensor	Coordinate	Sensor	Coordinate
S1	(-250,0)	S4	(0,250)	S7	(250,0)	S10	(0,-250)
S2	(-216.5,125)	S5	(125,216.5)	S8	(216.5,-125)	S11	(-125,-216.5)
S3	(-125,216.5)	S6	(216.5,125)	S9	(125,-216.5)	S12	(-216.5,-125)

B. Experiment to Simulated Damage

The size of the simulated damage specimen was 800 × 800 × 2.4 mm (Fig. 8). Table IV lists the coordinates of the sensors. The five-cycle Hanning-window-modulated sine wave with an amplitude of 60 V was used as the excitation signal. Based on the numerical simulation results of UGW dispersion, 70 kHz was selected as the center frequency of the excitation signal in the nondispersive region. The polling excitation method was used to excite Lamb wave signals to S1–S12 of the healthy plate, and a spherical damped soil [6], [36] with a diameter of 15 mm was used to simulate the damage at different locations.

汉窗

损伤模拟

C. Experiment to Impact Damage

The size of the impact damage specimen was 500 × 500 × 2.4 mm [Fig. 10(c)]. Table V lists the coordinates of the sensors. First, the specimen was fixed on the test bench base,

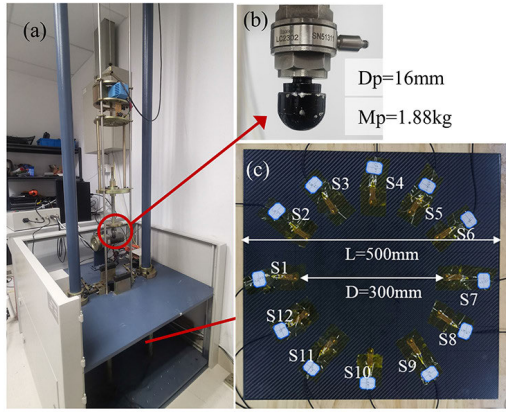


Fig. 10. Impact test system: (a) impact testing machine; (b) punch; and (c) impact testing specimen.

TABLE V
COORDINATES OF PZT SENSORS PASTED ON (UNIT: mm)

Sensor	Coordinate	Sensor	Coordinate	Sensor	Coordinate	Sensor	Coordinate
S1	(-150,0)	S4	(0,150)	S7	(150,0)	S10	(0,-150)
S2	(-129.9,75)	S5	(75, 129.9)	S8	(129.9,- 75)	S11	(-75,- 129.9)
S3	(-75, 129.9)	S6	(129.9, 75)	S9	(75,- 129.9)	S12	(-129.9,- 75)

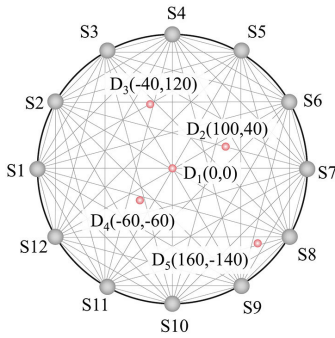


Fig. 11. Damage distribution in pre-experiments (unit: mm).

and the healthy signal was obtained under a nondestructive condition. Subsequently, the spherical damped soil with a diameter of 15 mm was placed at (0 mm, 50 mm), and UGW signals with damage information were obtained. Next, the impact damage test is performed. As depicted in Fig. 10, the model of the falling hammer impact tester was ZBG-0309, and the punch referred to a hemisphere with a diameter of 16 mm and a mass of 1.888 kg. The impact energy was set to 10 J. Finally, the signal of the ultrasonic guide wave containing the damage information was obtained. The excitation signal parameters were consistent with those of the simulated damage experiments.

IV. SIGNAL ANALYSIS AND PARAMETER OPTIMIZATION

In this section, the key steps and parameters mentioned in the algorithm are analyzed and discussed (e.g., group velocity correction, path optimization parameter α , ellipse scaling parameter β , and order of the algorithm) based on five random experimental observations (Fig. 11).

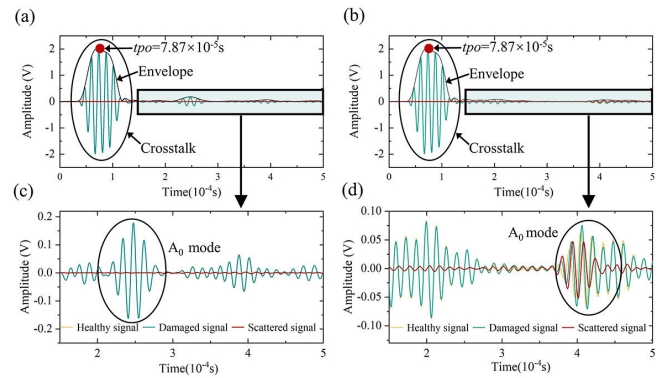


Fig. 12. Comparison of health signal, damage signal, and scattering signal: (a) path away from the damage: S1-S2; (b) path near the damage: S1-S6; (c) local amplified signal of path S1-S2; and (d) local amplified signal of S1 path S1-S6.

A. Effective Path Optimization: Threshold α

In general, damage in the plate has a limited range of effects on UGW. The scattering signal can directly observe the effect. Fig. 12 presents the healthy signal, the damage signal, and the scattered signal when the damage occurs at position D1(0 mm, 0 mm). As depicted in Fig. 12(a) and (b), the Hilbert transform is used to find the peak time of the crosstalk signal located at 7.87×10^{-5} s. The crosstalk signal is attributed to the high-voltage power amplifier of the system, and it is synchronized with the excitation signal while not interfering with the scattered signal. For the sake of observation, we zoom in to show the signal after 1.5×10^{-4} s and do not show the crosstalk signal in the subsequent section. As depicted in Fig. 12(d), the path adjacent to the damage usually expresses more robust damage information, termed the effective path. As depicted in Fig. 12(c), the path far from the damage has a weak scattered signal, termed the invalid path. The scattered wave packet of the invalid path fails to extract the time information accurately, and it will lead to the generation of computational errors, such that it needs to be removed to avoid errors.

The ratio of the scattered signal energy to the baseline signal energy is defined to express the degree of scattered energy change introduced by the damage and to eliminate the baseline effect. Subsequently, a threshold α is set for effective path screening, which is expressed in (24)

$$E_i = \frac{\text{Energy}(c_i - b_i)}{\text{Energy}(b_i)} \quad (23)$$

$$E_{oi} = \frac{E_i - E_{\min}}{E_{\max} - E_{\min}} \geq \alpha. \quad (24)$$

Fig. 13(a) presents E_o of the 66 paths in a healthy state and a damaged state [coordinates: D1(0 mm, 0 mm)]. It shows that the scattering energy index in the region near damage is significantly higher than the region far from damage. The larger the α , the more stable the scattered signal carries the damaged information, but the reduction of effective paths will pose a risk for damage localization. Therefore, a reasonable value of α will increase the robustness of the algorithm against environmental noise and uncontrollable biases of the system.

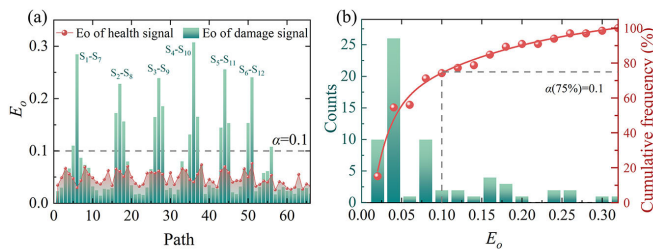


Fig. 13. Path optimization based on E_o : (a) E_o of damage D1 and (b) histogram of probability distribution and frequency accumulation curve of E_o .

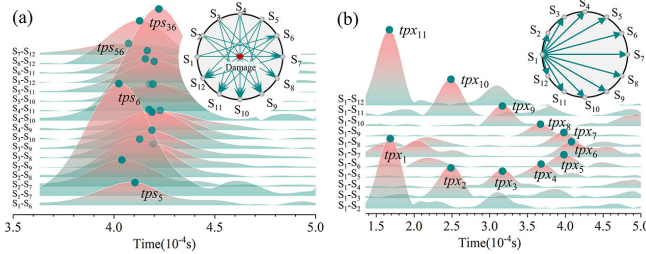


Fig. 14. Calculate t_{ps} and t_{px} of the effective scattering signal: (a) t_{ps} of the effective scattering signal and (b) t_{px} of health signal.

The E_o of the health signal shows that when $\alpha = 0.1$, the damage-independent paths can be filtered out directly. Finally, α 选择 25% of the effective paths are retained [Fig. 13(b)].

B. Modification of Group Velocity

Equation (11) suggests that the accurate calculation of t_s and t_x is the prerequisite for obtaining the MDF, where t_s is obtained by subtracting the wave packet peak time t_{ps} of the scattered signal and t_0 (7.87×10^{-5} s) of the excitation signal. Take damage D1(0 mm, 0 mm) as an example. The scattered signal after performing path screening is subjected to the Hilbert transform to obtain the signal envelope. Then, t_{ps} is obtained [Fig. 14(a)]. The calculation of t_x is determined by the accuracy of the modified group velocity c_{ga} and c_{gr} . In practical applications, the parameters (e.g., elastic modulus and shear modulus of the structure to be measured) are often difficult to know accurately, such that the velocity modification function obtained from the numerical simulation directly will introduce errors. The experimental health signal is adopted to conduct the effective scattering signal correction of group velocity in different propagation directions to solve the dependence on the material's prior parameters. The tof of the A0 mode is determined by subtracting the mode peak time t_{px} and t_0 (7.87×10^{-5} s) of the excitation signal. Taking the 11 paths excited by S1 and received by S2–S12 as an example, the Hilbert transform is performed to find the signal envelope to obtain t_{px} [Fig. 14(b)].

Based on the tof for either path and the sensor pair's distance d_s , the group velocity of the A0 mode in this direction can be calculated as follows:

$$c_{gi} = \frac{d_s}{tof_i}. \quad (25)$$

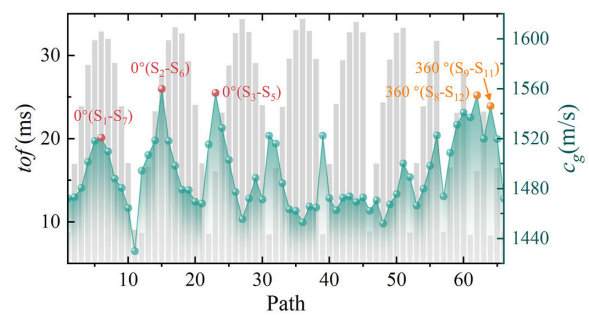


Fig. 15. Group velocity calculation of tof and c_g .

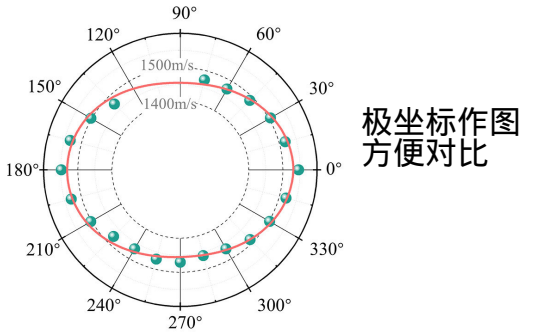


Fig. 16. Corrected group velocity in all the directions after fitting.

Fig. 15 presents the calculated results of tof and c_g for the 66 paths. The UGW propagating along 0° and 360° achieved the fastest group velocities. Then, the measured velocities are grouped by angle, and the corresponding average velocities c_{gc} of the respective angle are calculated. Furthermore, the polar plot with the fit curve (26) shown in Fig. 16 is fit. The trend of the group velocity variation is approximately equal to the numerical simulation results in Fig. 3

$$f(\theta) = 1454 + 76 \left(\sin\left(\frac{(\theta - 89)\pi}{184}\right) \right)^2, \quad 0 \leq \theta \leq 360. \quad (26)$$

C. Probabilistic Imaging of Paths: Scaling Parameter β

Parameter β controls the scaling rate of the probability distribution function, which is generally determined based on experience. With damage D2(100 mm, 40 mm) as an example, the probability densities under path S1–S6 are obtained using the PDI and MDF-PDI methods ($\beta = 0.1, 0.2, 0.3$), respectively (Fig. 17). As indicated by the result, the damage probability of damage D2 is increased with the increase in β in classical PDI method, suggesting that the value of β more significantly affects the localization results, consistent with previous studies. For the MDF-PDI method, no matter how β changes, D2 is constantly located at the position with the highest probability of damage. The localization accuracy depends more on the accuracy of τ_d than on the value of β . Accordingly, the experience-dependent fuzzy selection can achieve accurate localization, thus improving the fault tolerance of the algorithm, which is also an advantage of the

通过
实验
修正
速度

如何修正
？
为何不直
接测量速
度？

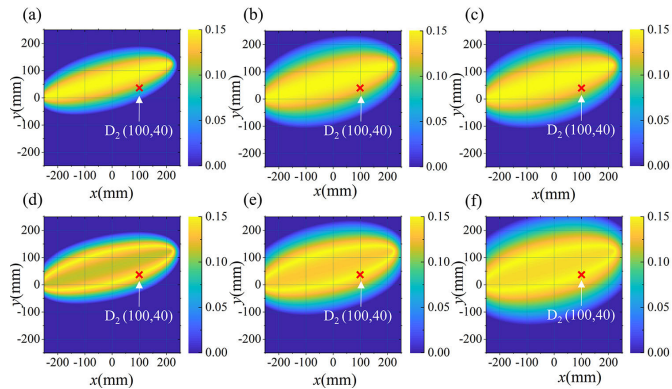


Fig. 17. Probability distribution of S1–S6 path for the PDI and MDF-PDI algorithms with different β : (a) PDI with $\beta = 0.1$; (b) PDI with $\beta = 0.2$; (c) PDI with $\beta = 0.3$; (d) MDF-PDI with $\beta = 0.1$; (e) MDF-PDI with $\beta = 0.2$ and (f) MDF-PDI with $\beta = 0.3$.

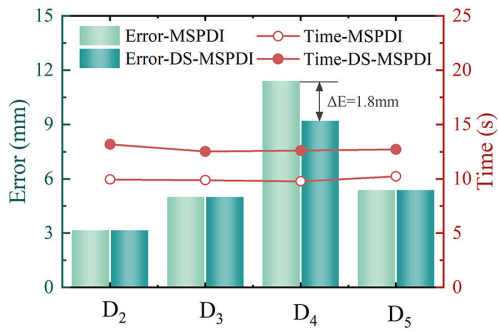


Fig. 18. Error and calculation time of the MSPDI and DS-MSPDI algorithms.

proposed algorithm. Thus, 0.2 serves this method as the value of β , which is determined by fuzzy selection.

D. Optimal Order Verification of MSPDI

In general, the double stage of the MSPDI method (DS-MSPDI) exhibits stronger damage focusing and noise suppression ability, whereas the disadvantage is that it generates more time loss. For certain damage $D(x_d, y_d)$ in the plane, the algorithm localizes the results $L(x_l, y_l)$, thus defining the absolute error

$$\text{Error} = \sqrt{(x_l - x_d)^2 + (y_l - y_d)^2}. \quad (27)$$

Validation is performed using four randomized damages (D2–D5) in pre-experiments. As indicated by the result (Fig. 18), DS-MSPDI obtains more accurate localization results than MSPDI while converging to the best in the first order. The algorithm is determined as the first order by balancing the time loss and localization accuracy.

V. RESULTS AND DISCUSSION

A. Localization Performance Verification for Simulated Damage

In the simulated damage experiment, 88 damages (Fig. 19) are randomly simulated in quadrants 1–4. They are divided into set A (including 80 damages inside the sensing arrays) and set B (covering eight damages at the edge of the sensing

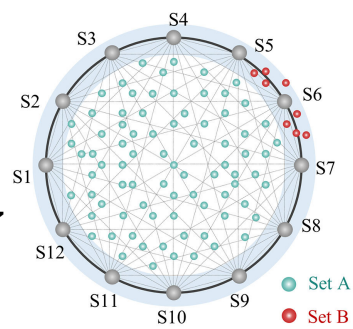


Fig. 19. Damage distribution of sets A and B.

TABLE VI
DEFINITION OF THE FOUR ALGORITHMS

Number	Algorithms	Group velocity modification	Probability accumulation method
1	DF-PDI	No	Sum
2	MDF-PDI	Yes	Sum
3	DF-MSPDI	No	Multiply-sum
4	MDF-MSPDI	Yes	Multiply-sum

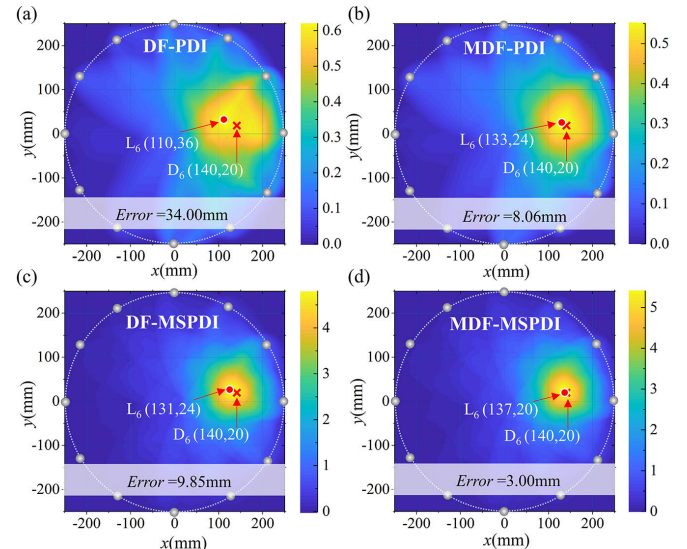


Fig. 20. Imaging results of internal damage D₆ (140, 20 mm): (a) DF-PDI; (b) MDF-PDI; (c) DF-MSPDI; and (d) MDF-MSPDI.

arrays). The definition of the above-mentioned damage follows the principles: 1) random uniform distribution and 2) including a wide variety of points of passing paths, deviating paths, passing path intersections, and deviating path intersections.

With the example of random damage D₆ (140 mm, 20 mm) incorporated into the sensing arrays, the imaging results and localization deviations of four algorithms are presented (Table VI). As depicted in Fig. 20, the localization error: MDF-MSPDI (3.00 mm) < MDF-PDI (8.06 mm) < DF-MSPDI (9.85 mm) < DF-PDI (34.00 mm). The result suggests that both group velocity modification and multiply-sum processing can increase the detection accuracy.

In the probability distribution form of the classical PDI method, the localization center diverges outward from the ellipse axis, such that an overall probability distribution is

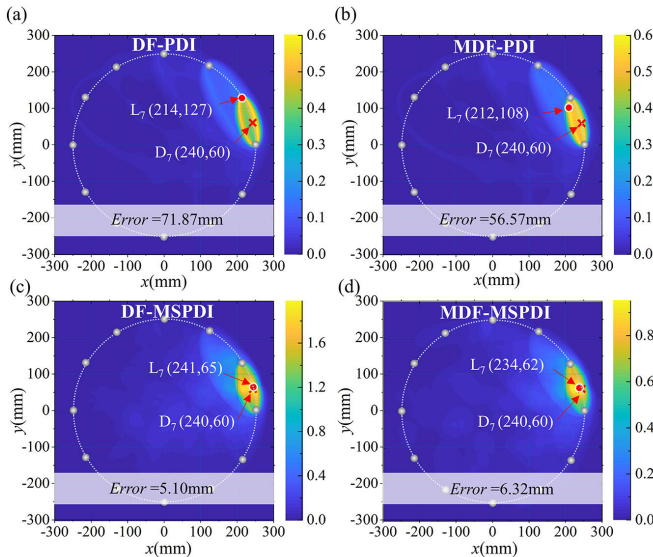


Fig. 21. Imaging results of edge damage D7 (140, 20 mm): (a) DF-PDI; (b) MDF-PDI; (c) DF-MSPDI; and (d) MDF-MSPDI.

generated, which is difficult to cover specific regions near sensors. The MDF method provides a ring-shaped probability distribution form that is advantageous for detecting edge damage. With the example of random damage D7 (140 mm, 20 mm), four algorithms' (Table VI) imaging results and localization deviations are presented (Fig. 21). The introduction of DF makes it possible for the PDI to detect damage outside the network, but it is inaccurate. The reason for this result is that when the damage is close to the edge of sensing network and other special locations, the reduction of the effective path will amplify the damage probability of certain 1–2 paths, thus leading to the generation of errors. In this case, the multiply–sum method increases the effective path by constructing a new probability distribution, thus accurately detecting edge damage.

To assess the overall performance of the algorithm, we define the MAE and STD

$$\text{MAE} = \frac{1}{m} \sum_{k=1}^m \text{Error}_k \quad (28)$$

$$\text{STD} = \sqrt{\frac{1}{m} \sum_{k=1}^m (\text{Error}_k - \overline{\text{Error}})^2} \quad (29)$$

where m is the number of damaged samples and $\overline{\text{Error}}$ is the mean deviation. MAE and STD are used to measure the trueness and the precision of the algorithm, respectively. For the two types of damage in sets A and B, we assessed the MAE and STD of the four algorithms (Fig. 22). For all 88 damages, the error's distribution and frequency accumulation curve are shown in Fig. 23.

The following conclusions are drawn through an analysis combining Figs. 22 and 23: 1) the proposed MDF-MSPDI algorithm's performance is clearly superior. It has a very accurate and stable capability for damage detection of anisotropic; 2) the localization performance of set A is always better than that of set B. It is due to the higher number of effective paths for damage located inside the sensing network, which

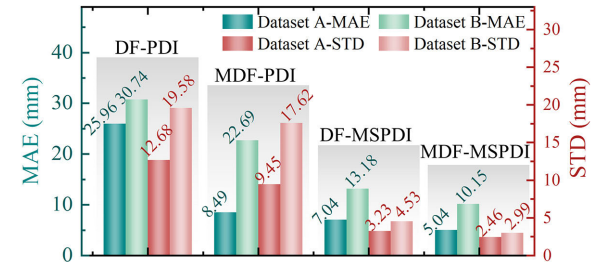


Fig. 22. MAE and STD indices for sets A and B.

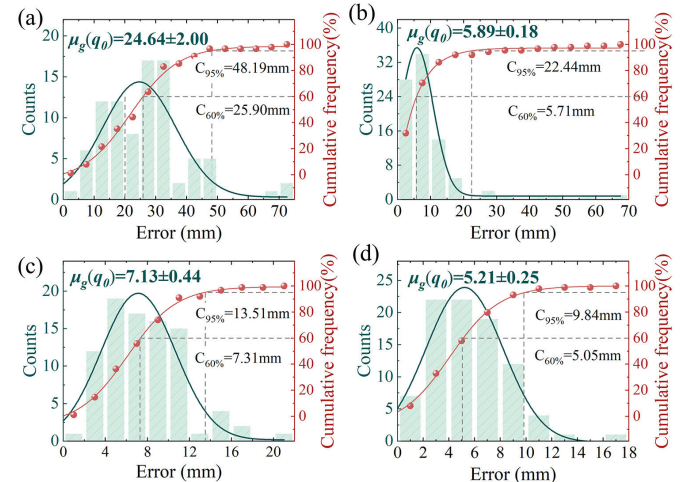


Fig. 23. Frequency distribution and cumulative frequency of positioning errors: (a) DF-PDI; (b) MDF-PDI; (c) DF-MSPDI; and (d) MDF-MSPDI.

can provide more robust damage guidance; 3) the localization accuracy of MSPDI is much higher than that of PDI. The spatial auto-correlation operation used in the MSPDI method is capable of significantly controlling the errors correlated with measurement accuracy, feature extraction quality, and prior knowledge accuracy. This advantage gives it an edge in composite laminate inspection; and 4) DF-MSPDI outperforms MDF-PDI in localization accuracy, suggesting that the MSPDI method can significantly eliminate velocity errors. It is possible to obtain high positioning accuracy without group velocity modification, thus significantly enhancing its engineering applicability.

B. Localization Performance Verification of Impact Damage

The UGW signals of simulated and impact damage are obtained near the point (0 mm, 50 mm) [Fig. 24(a)]. An ultrasonic PA detection system is adopted to obtain the 2-D C-scan [Fig. 24(c)] and S-scan [Fig. 24(d)] images of the impact damage, so as to obtain damage information more intuitively. The host is a portable ultrasonic PA flaw detector (OmniScan MX2, Olympus). The phased array probe is a linear array near-wall probe (5L64-NW1) with a center frequency of 5 MHz. The center of the impact damage is measured as (-2 mm, 53 mm) [Fig. 24(b)].

Based on the comparison of the UGW signals under simulated and impact damage conditions, local amplification of the A0 wave is performed, i.e., the main concern. As depicted in Fig. 25(a), neither the simulated nor the impact damage significantly affects the signal of the invalid path. This weak

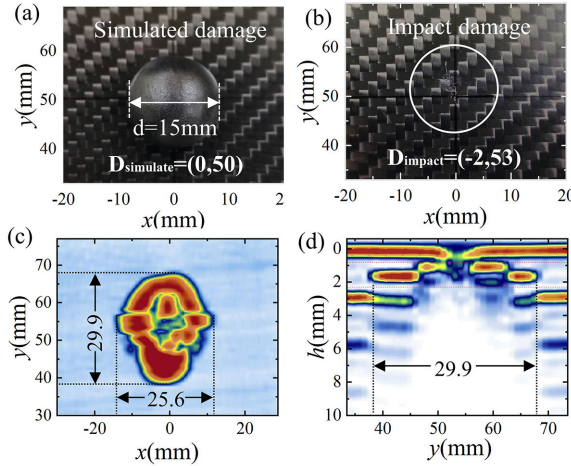


Fig. 24. Location and size of impact damage: (a) location and size of damage simulated by damped soil; (b) location of impact damage; (c) C-scan images of impact damage; and (d) S-scan images of impact damage.

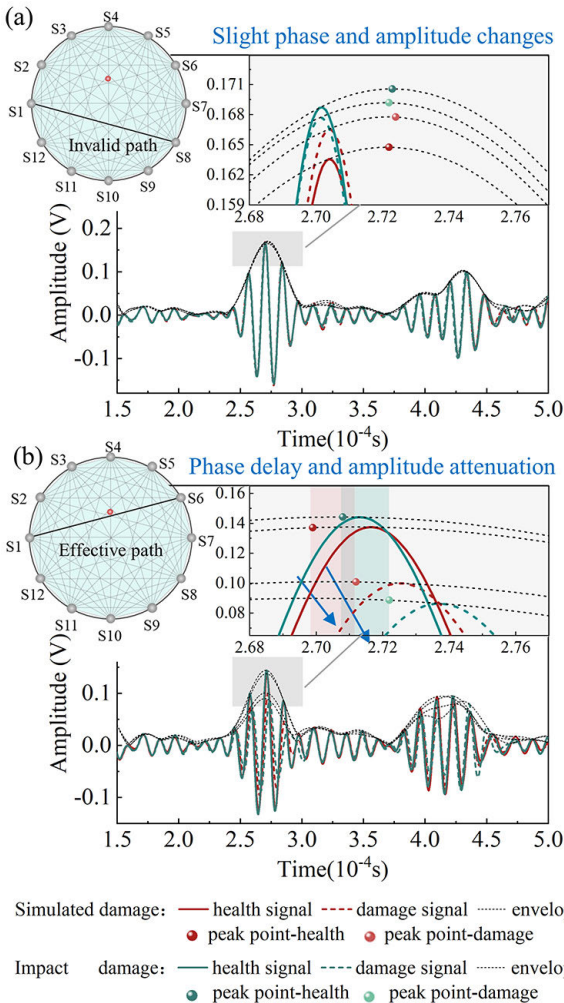


Fig. 25. Changes in the phase and amplitude characteristics of the signal: (a) invalid path and (b) effective path.

phase or amplitude drift arising from environmental noise and differences in boundary conditions is negligible. In Fig. 25(a), the occurrence of damage triggers phase delay and amplitude decay of the effective path, consistent in simulated and real

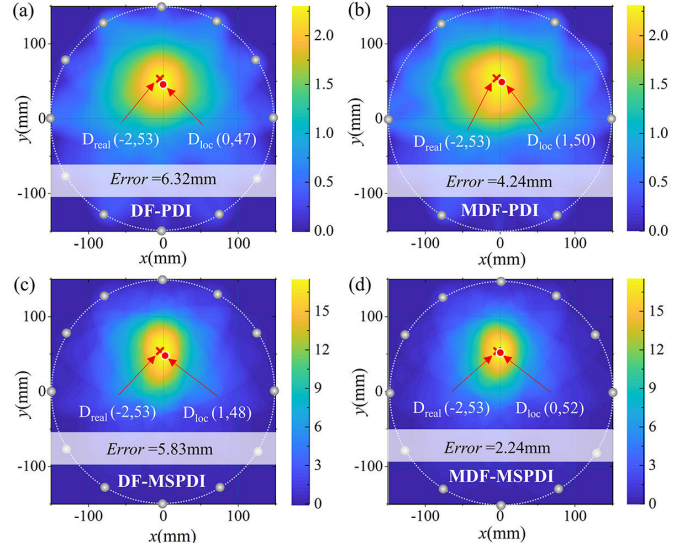


Fig. 26. Imaging results of impact damage $D_{\text{impact}} (-2, 53 \text{ mm})$: (a) DF-PDI; (b) MDF-PDI; (c) DF-MSPDI; and (d) MDF-MSPDI.

damage. As revealed by the above result, it is feasible to simulate the actual damage by damped soil.

A total of four algorithms' imaging results are presented for the damage $D_{\text{impact}} (-2 \text{ mm}, 53 \text{ mm})$ obtained from the impact test. As depicted in Fig. 26, the localization error: MDF-MSPDI (2.24 mm) < MDF-PDI (4.24 mm) < DF-MSPDI (5.83 mm) < DF-PDI (6.32 mm). The results show that both MDF and MSPDI can improve the localization accuracy, and the MDF-MSPDI has the highest accuracy.

The same conclusions are drawn for the impact and damping soil experiments, such that the statistics in Sections V-A and V-B can be adopted to assess the algorithm performance.

VI. CONCLUSION

In this study, an MDF-MSPDI algorithm is proposed to increase the detection accuracy and robustness in composite structures. The algorithm's performance is verified by simulated and impact damage experiments.

The probability distribution function is defined with the MDF of the scattered signal's backpropagation characteristics. The aim is to ensure that the algorithm exhibits a wide range of damage detection capabilities while avoiding errors introduced by empirical judgments of elliptical scaling parameter values. As indicated by the result, the anisotropy of group velocity in composite materials can increase the detection accuracy. The damaged images are reconstructed by coupled multiply-sum operation of the respective path imaging. The errors arising from the prior knowledge and computational accuracy are directly compensated by the spatial auto-correlation operation, such that the engineering application capability is significantly improved.

In the practical detection environment, changes in temperature and noise will affect the quality of damage imaging. Moreover, the presence of multiple impairments will hinder damage reconstruction. Thus, in our subsequent research, the environment compensation algorithm will be optimized, and the multidamage detection capability will be enhanced.

REFERENCES

- [1] Y. Gong, L. Zhao, J. Zhang, N. Hu, and C. Zhang, "An insight into three approaches for determining fatigue delamination resistance in DCB tests on composite laminates," *Compos. B, Eng.*, vol. 176, Nov. 2019, Art. no. 107206.
- [2] B. Fazlali, S. V. Lomov, and Y. Swolfs, "Fiber break model for tension-tension fatigue of unidirectional composites," *Compos. B, Eng.*, vol. 220, Sep. 2021, Art. no. 108970.
- [3] O. Falcó, C. S. Lopes, D. E. Sommer, D. Thomson, R. L. Ávila, and B. H. A. H. Tijss, "Experimental analysis and simulation of low-velocity impact damage of composite laminates," *Compos. Struct.*, vol. 287, May 2022, Art. no. 115278.
- [4] J. Wu, X. Xu, C. Liu, C. Deng, and X. Shao, "Lamb wave-based damage detection of composite structures using deep convolutional neural network and continuous wavelet transform," *Compos. Struct.*, vol. 276, Nov. 2021, Art. no. 114590.
- [5] Y. He, Y. Xiao, Z. Su, Y. Pan, and Z. Zhang, "Contact acoustic nonlinearity effect on the vibro-acoustic modulation of delaminated composite structures," *Mech. Syst. Signal Process.*, vol. 163, Jan. 2022, Art. no. 108161.
- [6] H. Zhang, J. Hua, F. Gao, and J. Lin, "Efficient Lamb-wave based damage imaging using multiple sparse Bayesian learning in composite laminates," *NDT E Int.*, vol. 116, Dec. 2020, Art. no. 102277.
- [7] S. Boccardi, G. P. M. Fierro, and M. Meo, "Nonlinear ultrasonic imaging of damage in composite materials using a higher harmonic and modulated multi-path reciprocal method," *Struct. Health Monitor.*, vol. 20, no. 6, pp. 2953–2962, Nov. 2021.
- [8] H. Jin, J. Yan, X. Liu, W. Li, and X. Qing, "Quantitative defect inspection in the curved composite structure using the modified probabilistic tomography algorithm and fusion of damage index," *Ultrasonics*, vol. 113, May 2021, Art. no. 106358.
- [9] R. Sicard, A. Chahbaz, and J. Goyette, "Guided Lamb waves and L-SAFT processing technique for enhanced detection and imaging of corrosion defects in plates with small depth-to-wavelength ratio," *IEEE Trans. Ultrason., Ferroelectr., Freq. Control*, vol. 51, no. 10, pp. 1287–1297, Oct. 2004.
- [10] J. Hua, H. Zhang, Y. Miao, and J. Lin, "Modified minimum variance imaging of Lamb waves for damage localization in aluminum plates and composite laminates," *NDT E Int.*, vol. 125, Jan. 2022, Art. no. 102574.
- [11] A. Nokhbatolfoghaei, H. M. Navazi, and R. M. Groves, "Evaluation of the sparse reconstruction and the delay-and-sum damage imaging methods for structural health monitoring under different environmental and operational conditions," *Measurement*, vol. 169, Feb. 2021, Art. no. 108495.
- [12] W.-J. Yan, D. Chronopoulos, C. Papadimitriou, S. Cantero-Chinchilla, and G.-S. Zhu, "Bayesian inference for damage identification based on analytical probabilistic model of scattering coefficient estimators and ultrafast wave scattering simulation scheme," *J. Sound Vibrat.*, vol. 468, Mar. 2020, Art. no. 115083.
- [13] A. Bayoumi, T. Minten, and I. Mueller, "Determination of detection probability and localization accuracy for a guided wave-based structural health monitoring system on a composite structure," *Appl. Mech.*, vol. 2, no. 4, pp. 996–1008, Dec. 2021.
- [14] C. Zhou, Z. Su, and L. Cheng, "Quantitative evaluation of orientation-specific damage using elastic waves and probability-based diagnostic imaging," *Mech. Syst. Signal Process.*, vol. 25, no. 6, pp. 2135–2156, Aug. 2011.
- [15] C. Zhou, Z. Su, and L. Cheng, "Probability-based diagnostic imaging using hybrid features extracted from ultrasonic Lamb wave signals," *Smart Mater. Struct.*, vol. 20, no. 12, Dec. 2011, Art. no. 125005.
- [16] D. Wang, L. Ye, Y. Lu, and F. Li, "A damage diagnostic imaging algorithm based on the quantitative comparison of Lamb wave signals," *Smart Mater. Struct.*, vol. 19, no. 6, Jun. 2010, Art. no. 065008.
- [17] D. Wang, L. Ye, Y. Lu, and Z. Su, "Probability of the presence of damage estimated from an active sensor network in a composite panel of multiple stiffeners," *Compos. Sci. Technol.*, vol. 69, no. 13, pp. 2054–2063, Oct. 2009.
- [18] Z. Wu, K. Liu, Y. Wang, and Y. Zheng, "Validation and evaluation of damage identification using probability-based diagnostic imaging on a stiffened composite panel," *J. Intell. Mater. Syst. Struct.*, vol. 26, no. 16, pp. 2181–2195, Nov. 2015.
- [19] H. Huo, J. He, and X. Guan, "A Bayesian fusion method for composite damage identification using Lamb wave," *Structural Health Monitor.*, vol. 20, no. 5, 2020, Art. no. 1475921720945000.
- [20] G. Liu, B. Wang, L. Wang, Y. Yang, and X. Wang, "Probability-based diagnostic imaging with corrected weight distribution for damage detection of stiffened composite panel," *Struct. Health Monitor.*, vol. 21, no. 4, pp. 1432–1446, Jul. 2022.
- [21] B. Zhang, X. Hong, and Y. Liu, "Deep convolutional neural network probability imaging for plate structural health monitoring using guided waves," *IEEE Trans. Instrum. Meas.*, vol. 70, pp. 1–10, 2021.
- [22] D. Wang, L. Ye, Z. Su, Y. Lu, F. Li, and G. Meng, "Probabilistic damage identification based on correlation analysis using guided wave signals in aluminum plates," *Struct. Health Monitor.*, vol. 9, no. 2, pp. 133–144, Nov. 2009.
- [23] C. H. Wang, J. T. Rose, and F.-K. Chang, "A synthetic time-reversal imaging method for structural health monitoring," *Smart Mater. Struct.*, vol. 13, no. 2, p. 415, 2004.
- [24] J. E. Michaels and T. E. Michaels, "Guided wave signal processing and image fusion for in situ damage localization in plates," *Wave Motion*, vol. 44, no. 6, pp. 482–492, Jun. 2007.
- [25] Z. Sharif-Khodaei and M. H. Aliabadi, "Assessment of delay-and-sum algorithms for damage detection in aluminium and composite plates," *Smart Mater. Struct.*, vol. 23, no. 7, Jul. 2014, Art. no. 075007.
- [26] M. S. Salmanpour, Z. S. Khodaei, and M. H. Aliabadi, "Transducer placement optimisation scheme for a delay and sum damage detection algorithm," *Struct. Control Health Monitor.*, vol. 24, no. 4, p. e1898, Apr. 2017.
- [27] Y. Liu, X. Hong, and B. Zhang, "A novel velocity anisotropy probability imaging method using ultrasonic guided waves for composite plates," *Measurement*, vol. 166, Dec. 2020, Art. no. 108087.
- [28] P. Zabbal, G. Ribay, B. Chapuis, and J. Jumel, "Multichannel multiple signal classification for dispersion curves extraction of ultrasonic guided waves," *J. Acoust. Soc. Amer.*, vol. 143, no. 2, pp. EL87–EL92, Feb. 2018.
- [29] C. Xu, Z. Yang, H. Zuo, and M. Deng, "Minimum variance Lamb wave imaging based on weighted sparse decomposition coefficients in quasi-isotropic composite laminates," *Compos. Struct.*, vol. 275, Nov. 2021, Art. no. 114432.
- [30] Y. Ren, L. Qiu, S. Yuan, and F. Fang, "Gaussian mixture model and delay-and-sum based 4D imaging of damage in aircraft composite structures under time-varying conditions," *Mech. Syst. Signal Process.*, vol. 135, Jan. 2020, Art. no. 106390.
- [31] B. Yang et al., "Damage localization in hydrogen storage vessel by guided waves based on a real-time monitoring system," *Int. J. Hydrogen Energy*, vol. 44, no. 40, pp. 22740–22751, Aug. 2019.
- [32] G. Matrone, A. Ramalli, P. Tortoli, and G. Magenes, "Experimental evaluation of ultrasound higher-order harmonic imaging with filtered-delay multiply and sum (F-DMAS) non-linear beamforming," *Ultrasonics*, vol. 86, pp. 59–68, May 2018.
- [33] C. Lou, M. Yuchi, and M. Ding, "Double stage delay multiply and sum beamforming combined with full-lag spatial coherence in ultrasound imaging," in *Proc. IEEE 6th Int. Conf. Signal Image Process. (ICSIP)*, Oct. 2021, pp. 416–420.
- [34] C. Yilmaz et al., "Non-destructive determination of the stiffness matrix of a laminated composite structure with Lamb wave," *Compos. Struct.*, vol. 237, Apr. 2020, Art. no. 111956.
- [35] M. Rautela and S. Gopalakrishnan, "Ultrasonic guided wave based structural damage detection and localization using model assisted convolutional and recurrent neural networks," *Exp. Syst. Appl.*, vol. 167, Apr. 2021, Art. no. 114189.
- [36] J. Zhu, X. Qing, X. Liu, and Y. Wang, "Electromechanical impedance-based damage localization with novel signatures extraction methodology and modified probability-weighted algorithm," *Mech. Syst. Signal Process.*, vol. 146, Jan. 2021, Art. no. 107001.



Lingyu Sun received the B.S. degree from the Department of Control Science and Engineering, Shandong University, Jinan, China, in 2018, where she is currently pursuing the Ph.D. degree with the School of Control Science and Engineering.

Her current research interests include nondestructive damage detection.



Juntao Wei received the B.S. and M.S. degrees from the Department of Control Science and Engineering, Shandong University, Jinan, China, in 2015 and 2018, respectively, where he is currently pursuing the Ph.D. degree with the School of Control Science and Engineering.

His current research interests include nondestructive damage detection and instrument techniques.



Faye Zhang received the B.S., M.S., and Ph.D. degrees from the Department of Control Science and Engineering, Shandong University, Jinan, China, in 2006, 2009, and 2017, respectively.

He is currently an Engineer with the Department of Control Science and Engineering, Shandong University. His current research interests include optical fiber sensors and their applications.



Chang Peng received the Ph.D. degree from the College of Mechanical and Vehicle Engineering, Chongqing University, Chongqing, China, in 2014.

He is currently a Senior Engineer at the National Engineering Research Center for High-Speed EMU of CRRC, Qingdao Sifang Company Ltd., Qingdao, China. His current research interests include fault prediction and structural health monitoring.



Lei Zhang received the B.S. and Ph.D. degrees from Tianjin University, Tianjin, China, in 2009, and 2014, respectively.

He studied on exchange at the Institute of Experimental Physics, John Kepler Linz University, from 2013 to 2014. He is currently an Associate Professor at the School of Control Science and Engineering, Shandong University, Jinan, China. His current research interests include study of novel sensors and their systems.



Zengye Ju received the B.S. degree from the Qingdao University of Technology, Qingdao, China, in 2010, and the M.S. degree from Central South University, Changsha, China, in 2013.

He is currently a Research and Development Engineer at the National Engineering Technology Research Center for High-Speed Rolling Stock Assembly of CRRC, Qingdao Sifang Company Ltd., Qingdao. His current research interests include structural health monitoring and safety assessment of rail vehicles.



Lei Jia received the B.S. degree in electrical engineering and automation from Shandong Polytechnic University, Jinan, China, in 1982, the M.S. degree in industrial automation from Shandong University, Jinan, in 1988, and the Ph.D. degree in automation from Zhejiang University, Hangzhou, China, in 1993.

In 1993, he joined Shandong Polytechnic University, where he has been a Professor, since 1995. In 1999, he was with Shandong University, as a Professor with the School of Control Science and

Engineering. His research interests mainly include intelligent detection technology, advanced ocean sensing technology, structural health monitoring, and seawater desalination.



Shanshan Lv received the Ph.D. degree from the Institute of Marine Science and Technology, Shandong University, Qingdao, China, in 2020.

She is currently a Post-Doctoral with the School of Control Science and Engineering, Shandong University, Jinan, China. Her current research interests include vision and ultrasonic guided wave-based damage detection.



Mingshun Jiang (Member, IEEE) received the B.S. and Ph.D. degrees from the Department of Control Science and Engineering, Shandong University, Jinan, China, in 2004, and 2010, respectively.

He is currently a Professor at the School of Control Science and Engineering, Shandong University. His current research interests include intelligent sensors, structural health monitoring, fault diagnosis, digital twin and visualization, and big data analysis.